PRAMANA
— journal of
physics

Vol. 59, No. 1
July 2002
pp. 91–111

Control of a coupled map lattice model for vortex shedding in the wake of a cylinder

G BALASUBRAMANIAN, D J OLINGER and M A DEMETRIOU
Mechanical Engineering Department, Worcester Polytechnic Institute, Worcester, MA 01609-2280, USA
Email: gana@wpi.edu; olinger@wpi.edu; mdemetri@wpi.edu

MS received 17 October 2001

Abstract. The flow behind a vibrating flexible cable at low Reynolds numbers can exhibit complex wake structures such as lace-like patterns, vortex dislocations and frequency cells. These structures have been observed in experiments and numerical simulations, and are predicted by a previously developed low-order coupled map lattice (CML). The discrete (in time and space) CML models consist of a series of diffusively coupled circle map oscillators along the cable span. Motivated by a desire to modify the complex wake patterns behind flexible vibrating cables, we have studied the addition of control terms into the highly efficient CML models and explored the resulting dynamics. Proportional, adaptive proportional and discontinuous non-linear (DNL) control methods were used to derive the control laws. The first method employed occasional proportional feedback. The adaptive method used spatio-temporal feedback control. The DNL method used a discontinuous feedback linearization procedure, and the controller was designed for the resulting linearized system using eigenvalue assignment. These techniques were applied to a modeled vortex dislocation structure in the wake of a vibrating cable in uniform freestream flow. Parallel shedding patterns were achieved for a range of forcing frequency-forcing amplitude combinations studied to validate the control theory. The adaptive proportional and DNL methods were found to be more effective than the proportional control method due to the incorporation of a spatially varying feedback gain across the cylinder span. The DNL method was found to be the most efficient controller of the low-order CML model. The required control level across the cable span was correlated to the 1/1 lock-on behavior of the temporal circle map.

Keywords. Non-linear dynamics; coupled map lattices; control of chaos; adaptive control; vortex shedding; flow control.

PACS Nos 05.45.-a; 05.45.Gg; 05.45.Ra; 47.27.Vf; 47.62.+q

1. Introduction

The wake of a circular cylinder at low Reynolds number is characterized by a vortex street where vortices are shed alternatively from each side of the cylinder surface. This arrangement causes an alternating pressure force and periodically fluctuating lift and drag forces leading to bluff body vibration. Vortex shedding is a classical fluid flow that has been well-studied for over a century [1,2]. Even with this sustained investigation, a complete understanding of the physics of this complicated phenomenon has defied explanation, even in the

low Reynolds number regime studied in this paper. A recent focus intended to address this issue, the so-called *dynamical systems approach*, has used low-order iterative dynamical systems to model cylinder wakes. For example, it has been shown that low-dimensional iterative models, such as the circle map, can predict the wake of a rigid oscillating circular cylinder [3]. The circle map [3–5]

$$\theta_{n+1} = \theta_n + \Omega - \frac{K}{2\pi}\sin(2\pi\theta_n), \tag{1}$$

was used to study a cylinder wake subjected to an imposed oscillation of controlled amplitude and frequency. The circle map is a standard universal model describing the dynamics of two coupled oscillators on a Poincaré section. The parameters in the circle map can be related to the wake situation as follows: The system variable θ_n represents the phase of the vortex shedding event at discrete times $t = n\Delta t = n/f_e$. The periodic vortex shedding from a stationary cylinder (at frequency f_{so}) and the imposed cylinder oscillation (at f_e) yield the unforced frequency ratio, $\Omega = f_{so}/f_e$. The parameter K is analogous to the imposed cylinder oscillation amplitude, A/D, where A is the amplitude and D is the cylinder diameter.

In a related approach, Olinger [6] has developed a low-order coupled map lattice (CML) model, based on a series of diffusively coupled circle map oscillators along the cylinder span. The CML model can predict complex vortex shedding patterns in the wake of forced flexible cables. The complex wake structures such as vortex dislocations, lace-like patterns for standing wave cable shapes, and oblique shedding for traveling waves along the cable span were initially observed in these simulations. More details of this low-order model will be provided in subsequent discussion. The flow-induced vibration of an elastic, cylindrical structure such as a flexible cable is a flow of fundamental importance where many issues remain unresolved. While several investigators have focused on wakes behind vibrating cables [7,8], the work of Newman and Karniadakis [9,10] is the most relevant here. Newman and Karniadakis have studied vortex shedding patterns in the wake of an oscillating cable at low Reynolds number using spectral element computations. Comparisons between predictions of the CML model and the spectral element computations have been made in [6].

We should point out that previous investigators have studied coupled circle map oscillators. For example, Kaneko [11,12] investigated coupled map lattices as a model for spatiotemporal chaos and made some connections with the Navier–Stokes equations. Kaneko also has studied transitions among coherent, ordered, partially ordered and turbulent states in circle maps. Olinger [6] represented the first attempt to model wake flow dynamics directly with coupled circle maps.

The advantage of such an approach is that the developed low-order models provide an alternative to solving the complex Navier–Stokes equations that govern the fluid flow. At first site, it appears surprising that there should be a correspondence between these low-order models and a fluid system that is governed by partial differential equations such as the Navier–Stokes equations. This correspondence can be attributed to an important property of dissipative systems such as those governed by the viscous Navier–Stokes equations. Viscous dissipation stabilizes orbital instability, contracts the phase space, and thereby allows some high-dimensional systems, under certain circumstances, to assume low-dimensional characteristics [13]. For example, connections between the circle map and the Navier–Stokes equations can be established using a Landau–Stuart equation [14,15] as a starting point. The Landau–Stuart equation can be deduced from the Navier–Stokes equations, and

is known to describe the wake evolution under appropriate conditions, e.g., near the critical Reynolds number for vortex shedding where the wake undergoes a Hopf bifurcation and takes on low-dimensional characteristics [16–18]. Of course, low-order systems such as the CML model have certain limitations. For example, at the current state of development, the models depend heavily on knowledge gained from previous experiments and numerical simulations on wake flows. Further discussion of these limitations can be found in [6].

Motivated by a desire to modify the complex wake patterns behind flexible vibrating cables, we study the addition of control terms into the CML models and explore the resulting dynamics. The control of three-dimensional wake patterns in the wake of circular cylinders has been an area of recent focus in experimental work [19,20]. As in the present work, the goal has often been to modify the complex wake pattern to achieve a vortex shedding pattern oriented in parallel with the cylinder axis.

The control of wake patterns has both fundamental and practical consequences. It is often possible to obtain a fundamental understanding of fluid dynamic mechanisms at work when a control method is applied. On the practical side, control of wake patterns behind bluff bodies can lead to drag and noise reduction, or altered cable-wake coupling (and hence vibration amplitude) in the case of a flexible cable.

Specific to the present work, addition of control terms into the coupled map lattice constitutes the first step towards the use of the CML models in flow control applications for wake flows. The eventual goal is to run the highly efficient CML models with added control terms in parallel with a laboratory wake experiment in which a flexible cable is induced to vibration by an oncoming freestream flow. The primary variable in the CML, the phase of vortex shedding, can be sensed in an experiment through standard hot-film velocity measurement techniques [21]. As a result, the couple map lattice studied in this work could model the wake flow in a feedback control system designed to produce desired wake patterns behind the vibrating cable. The present study does not yet address certain practical control issues, such as the method of control actuation for wake forcing, but instead focuses solely on the dynamics of the new CML models.

The control of complex behaviors derived from low-dimensional dynamical systems has also been a topic of interest in recent years. For example, 'chaos control' techniques first proposed by Ott *et al* [22] use occasional proportional logic to stabilize unstable periodic orbits of a chaotic attractor. While the control of unpredictable, chaotic systems seems counter-intuitive at first, the fact that chaotic systems exhibit sensitive dependence on initial conditions means that small amplitude control inputs can have a substantial effect on final system states. Sinha and Gupta [23] investigated two-dimensional coupled map lattices and targeted spatio-temporal patterns using adaptive control techniques. Several investigators [24–26] have used control strategies motivated by [22] that are somewhat similar to the proportional control method applied in the present work. These investigations focused on control of chaos in a thermal convection loop. The desire to explore application of these techniques to the vortex shedding process using CML models is an additional motivation for this work. For comparison purposes adaptive proportional control scheme and discontinuous non-linear control scheme [27], which will be described in more detail in subsequent discussion, were also applied.

The paper is organized as follows: In §2 the previously developed coupled map lattice [6] is summarized. A description of the proportional control, adaptive proportional control and discontinuous non-linear control schemes applied to the CML model is presented in §3. The control of complex wake dynamics predicted by the CML model, using these control

schemes, is described in §4. The effectiveness of the three control schemes is studied focusing on wake patterns, in addition to both local and global dynamics of the wake and cable. A summary of results follows in §5.

2. Coupled map lattice

The coupled map lattice [6]

$$f_n^k = \widehat{X}_n^k + \Omega^k - K^k \sin(2\pi\widehat{X}_n^k - \phi^k - \pi/2)/2\pi, \quad k = 1, 2, \ldots, k^* \tag{2}$$

$$\widehat{X}_{n+1}^k = (1-2\varepsilon)\, f_n^k + \varepsilon\left(f_n^{k-1} + f_n^{k+1}\right), \tag{3}$$

is a discrete-time model that consists of the circle map [3–5] which models a cylinder (or flexible cable) wake with two competing frequencies, the shedding frequency (f_{so}) and excitation frequency (f_e). A simple diffusion model, eq. (3) provides spatial coupling between the k^* circle map oscillators placed along the cylinder span (see figure 1). Derivation of the diffusion model from a vorticity equation is detailed in [6]. In the circle map, $\widehat{X}_n^k$ is treated as modulo 1, and represents the phase of the vortex shedding process at discrete times $t = n\Delta t = n/f_e$ and span-wise location k. Appropriate boundary conditions at the cable ends can be established to model both periodic and non-periodic (sheared inflow) cases, although in the present work the focus is on the periodic cases.

The unforced frequency ratio $\Omega^k (= f_{so}^k/f_e)$ can vary with the span-wise location to model shear flow effects. However, in the present work uniform freestream flows ($\Omega =$ constant) are studied. The forcing term K^k models the cable oscillation amplitude (assumed

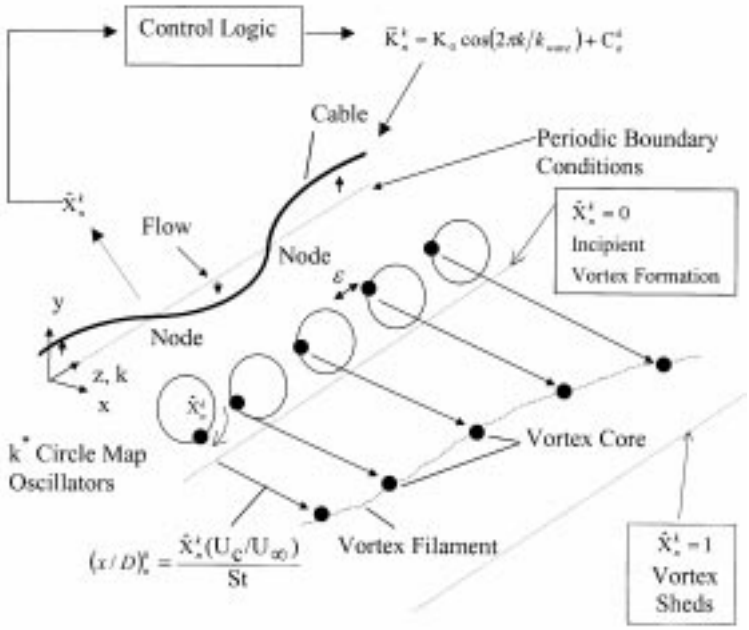

Figure 1. Schematic of the coupled map lattice model with added control terms. Adapted from [6].

to be in the y–z plane). The forcing term can be specified as a constant value along the cylinder span to model rigid cylinders. It can also vary sinusoidally, $K^k = K_0 \cos(2\pi k/k_{\text{wave}})$, to model the standing wave mode cable shapes considered in the present work. Specification of Ω^k and K^k in the coupled map lattice implies that externally forced, as opposed to self-excited, cable wakes are modeled in the present study. The input parameter ϕ^k in eq. (2) represents the phase angle between the vortex shedding event and the cylinder motion at a given location k. The diffusion coefficient ε in (3) provides the necessary coupling among the span-wise circle map oscillators, and is dependent on the Strouhal number St, Reynolds number Re, and L/D through $\varepsilon = \nu\Delta t/(\Delta z)^2 = \Omega^k(k^*-1)^2/(\text{St}\,\text{Re}(L/D)^2)$. Here L is the span-wise extent of the cable, D is the cylinder diameter, ν is the fluid kinematic viscosity and Δz is the spacing between circle map oscillators [6].

The primary output from the CML is the vortex shedding patterns (see figure 1). The phase of the vortex shedding $\widehat{X}_n^k$ is interpreted as follows to determine these patterns. A value of $\widehat{X}_n^k$ equal to 0 corresponds to incipient vortex formation (the start of the vortex formation process), while a value of $\widehat{X}_n^k$ equal to 1 corresponds to the vortex shedding event (the start of the next shedding cycle). The $\widehat{X}_n^k$ parameter is converted into downstream vortex core locations $(x/D)_n^k$ using the characteristic non-dimensional vortex spacing [6] in the stream-wise direction through $(x/D)_n^k = \widehat{X}_n^k x^* = \widehat{X}_n^k U_c/U_\infty \text{St}$. Here, U_c and U_∞ are vortex convection and freestream velocities respectively. By connecting the vortex cores at each of the k^* oscillator sites with vortex filaments, the wake vortex shedding pattern can be drawn (see figure 1). For a parallel shedding pattern that does not vary with time, $\widehat{X}_n^k = \overline{X}^k = \eta =$ constant. The wake pattern is assumed to develop in the near wake and convect downstream without any further evolution. Only a brief description of the CML model has been given here. Further details of this model can be found in [6].

3. Control methodology

In this section, we discuss certain features in the development of three coupled map lattice models where control terms are added (figure 1). The first model is based on occasional proportional control logic and aims to stabilize the unstable periodic orbits of a chaotic attractor [22]. The second model uses a linear adaptive proportional controller with a spatio-temporal feedback gain. The third model is based on a conditional feedback linearization of the non-linear coupled map lattice. The resulting linearized CML is controlled using eigenvalue assignment [27]. A summary of the control schemes is given in §3.1–§3.3.

3.1 *Proportional control*

The CML equations (2) and (3) are modified by the addition of a control signal C_n^k to the forcing term K^k, yielding

$$\widetilde{f}_n^k = \widehat{X}_n^k + \Omega^k - \widetilde{K}_n^k \sin(\psi_n^k)/2\pi, \tag{4}$$

$$\widehat{X}_{n+1}^k = (1-2\varepsilon)\,\widetilde{f}_n^k + \varepsilon(\widetilde{f}_n^{k-1} + \widetilde{f}_n^{k+1}), \tag{5}$$

where $\psi_n^k = 2\pi\widehat{X}_n^k - \phi_n^k - \pi/2$, $\widetilde{K}_n^k = K^k + C_n^k$. Comparing eq. (4) with eq. (2), we note that the phase angle between the vortex shedding event and the cylinder motion, ϕ_n^k, now varies with time since $\widetilde{K}_n^k$ varies through the term C_n^k. The magnitude of the control signal

$$C_n^k = \gamma\left(\widehat{X}_n^k - \overline{X}^k\right) \quad \text{or} \quad \mathbf{C}_n = \gamma\mathbf{I}\left(\widehat{\mathbf{X}}_n - \overline{\mathbf{X}}\right), \tag{6}$$

is proportional to the deviation of the system from the target pattern of vortex shedding $\overline{X}^k$. The feedback gain γ is constant in time and space [22,29].

3.2 *Adaptive proportional control*

This method represents an extension of the proportional control method. Here, each entry of the feedback gain $\widehat{\mathbf{\Gamma}}_n$ is assumed to be different from any other one, and thus through time adaptation of $\widehat{\mathbf{\Gamma}}_n$, the vector $\widehat{\mathbf{\Gamma}}_n = \left[\widehat{\Gamma}_n^1, \widehat{\Gamma}_n^2, \ldots, \widehat{\Gamma}_n^{k^*}\right]^T$ represents a temporally varying vector. Along with eqs (4) and (5), the following control law is used:

$$\mathbf{C}_n = \mathbf{H}(\widehat{\mathbf{X}}_n)\widehat{\mathbf{\Gamma}}_n, \quad \mathbf{H}(\widehat{\mathbf{X}}_n) = \operatorname{diag}\left(\widetilde{\boldsymbol{f}}_n\left(\widehat{\mathbf{X}}_n\right)\right) \quad \text{or} \quad C_n^k = \widehat{\Gamma}_n^k \widetilde{f}_n^k(\widehat{\mathbf{X}}_n). \tag{7}$$

In order to determine an update law for the feedback gain $\widehat{\mathbf{\Gamma}}_n$, we define the *state error* $\mathbf{X}$ as

$$\mathbf{X}_{n+1} = \widehat{\mathbf{X}}_{n+1} - \overline{\mathbf{X}}. \tag{8}$$

Our goal is to drive the state error to zero in the shortest possible time. We use a multivariable least squares algorithm [30] to minimize the state error after each time step. The following equations illustrate the steps in the derivation of the adaptation scheme for the feedback gain $\widehat{\mathbf{\Gamma}}_n$. The feedback gain can be updated by minimizing the cost function

$$J_n(\overline{\mathbf{\Gamma}}) = \frac{1}{2}\overline{\mathbf{\Gamma}}^T\mathbf{P}_0^{-1}\overline{\mathbf{\Gamma}} + \frac{1}{2}\sum_{j=1}^{n}\mathbf{X}_{j+1}^T\widetilde{\mathbf{R}}^{-1}\mathbf{X}_{j+1},$$

$$\widetilde{\mathbf{R}}^{-1} = \frac{\operatorname{diag}\left(\sin(\Psi_n)\right)\mathbf{R}^{-1}\operatorname{diag}\left(\sin(\Psi_n)\right)}{4\pi^2}, \tag{9}$$

where the dummy variable $\overline{\mathbf{\Gamma}}$ is used for analysis purposes only in place of $\widehat{\mathbf{\Gamma}}_n$. The parameters $\mathbf{P}_0^{-1}$ and $\mathbf{R}^{-1}$ are diagonal input weighting matrices and can be varied until optimal values are obtained. The equation

$$\frac{\partial}{\partial\overline{\mathbf{\Gamma}}}J_n(\overline{\mathbf{\Gamma}}) = \mathbf{0} \tag{10}$$

provides iteration for $\widehat{\mathbf{\Gamma}}_{n+1}$ with the adaptation proceeding in the direction of decreasing cost function. Next define

$$\mathbf{G}(\widehat{\mathbf{X}}_n) = \frac{\mathrm{diag}(\sin(\Psi_n))\mathbf{H}(\widehat{\mathbf{X}}_n)}{2\pi},$$
$$\mathbf{P}_n^{-1} = \left(\mathbf{P}_0^{-1} + \sum_{j=1}^{n} \mathbf{G}(\widehat{\mathbf{X}}_j)^T \mathbf{R}^{-1}\mathbf{G}(\widehat{\mathbf{X}}_j)\right)$$
$$= \left(\mathbf{P}_0^{-1} + \sum_{j=1}^{n} \mathbf{H}(\widehat{\mathbf{X}}_j)^T \widetilde{\mathbf{R}}^{-1}\mathbf{H}(\widehat{\mathbf{X}}_j)\right). \tag{11}$$

The feedback gain adaptation law is then given by

$$\mathbf{P}_n = \mathbf{P}_{n-1} - \mathbf{P}_{n-1}\mathbf{H}(\widehat{\mathbf{X}}_n)^T \left(\widetilde{\mathbf{R}} + \mathbf{H}(\widehat{\mathbf{X}}_n)\mathbf{P}_{n-1}\mathbf{H}(\widehat{\mathbf{X}}_n)^T\right)^{-1} \mathbf{H}(\widehat{\mathbf{X}}_n)\mathbf{P}_{n-1}, \tag{12}$$

$$\widehat{\mathbf{\Gamma}}_{n+1} = \widehat{\mathbf{\Gamma}}_n - \mathbf{P}_n\mathbf{H}(\widehat{\mathbf{X}}_n)^T \widetilde{\mathbf{R}}^{-1}\mathbf{X}_{n+1}, \tag{13}$$

where $\mathbf{P}_{-1} = \mathbf{P}_0$ is a known input weighting matrix for the state error $\mathbf{X}$. In addition to the techniques discussed in §3.2, we have used standard adaptive control techniques [30] including exponential data forgetting, covariance resetting etc.

3.3 *Discontinuous non-linear control*

In this method the control law is derived to send the state error to rest, so that, as $\mathbf{X}_{n\to\infty} \to \mathbf{0}, \widehat{\mathbf{X}}_{n\to\infty} \to \overline{\mathbf{X}}$. In the case of parallel shedding, $\overline{X}^k = \eta, \forall k = 1, 2, \ldots, k^*$, where η is a real constant. The modified coupled map lattice is written as

$$\widetilde{f}_n^k = \widehat{X}_n^k + \Omega^k - \widetilde{K}_n^k \sin(\psi_n^k)/2\pi, \tag{14}$$

$$\widehat{X}_{n+1}^k = (1-2\varepsilon)\,\widetilde{f}_n^k + \varepsilon\left(\widetilde{f}_n^{k-1} + \widetilde{f}_n^{k+1}\right), \tag{15}$$

where $\psi_n^k = 2\pi\widehat{X}_n^k - \phi_n^k - \pi/2$, $\widetilde{K}_n^k = K^k + C_n^k$.

With further manipulation,

$$X_{n+1}^k = (1-2\varepsilon)\left(X_n^k + u_n^k\right) + \varepsilon\left(X_n^{k+1} + u_n^{k+1}\right) + \varepsilon\left(X_n^{k-1} + u_n^{k-1}\right) \tag{16}$$

results, where the input term u_n^k is related to the forcing term $\widetilde{K}_n^k$ via $u_n^k = \Omega^k - \widetilde{K}_n^k \sin(\psi_n^k)/2\pi$. We can now write eq. (16) in vector form as $\mathbf{X}_{n+1} = \mathbf{A}(\mathbf{X}_n + \boldsymbol{u}_n)$ where $\mathbf{X}_n = \left[X_n^1, X_n^2, \ldots, X_n^{k^*}\right]^T$, $\mathbf{A}$ accounts for the spatial coupling and $\boldsymbol{u}_n = \left[u_n^1, u_n^2, \ldots u_n^{k^*}\right]^T$. The feedback gain matrix $\mathbf{G}$ is designed using a pole placement (eigenvalue assignment) [28] technique so that the control input is derived as $\boldsymbol{u}_n = -\mathbf{G}\mathbf{X}_n$ and the closed loop system becomes $\mathbf{X}_{n+1} = (\mathbf{A} - \mathbf{A}\mathbf{G})\,\mathbf{X}_n$. The model uses a conditional feedback linearization procedure, thereby providing for saturation of the control input using a threshold parameter β. The control input is limited to a threshold parameter α to ensure that the forcing term after control is limited as shown in eq. (18).

$$u_n^k = \begin{cases} -\mathrm{sgn}\left(\mathbf{G}^k\mathbf{X}_n\right) * \min\left(\left|\mathbf{G}^k\mathbf{X}_n\right|, \alpha\right), & \text{if } |\sin(\psi_n^k)| > \beta \\ \Omega^k - 1, & \text{if } |\sin(\psi_n^k)| \le \beta \end{cases}, \quad \mathbf{G}^k \text{ is the } k\text{th row of } \mathbf{G}, \tag{17}$$

$$\widetilde{K}_n^k = \begin{cases} -2\pi(u_n^k + 1 - \Omega^k)/\sin(\psi_n^k), & \text{if } |\sin(\psi_n^k)| > \beta \\ 0, & \text{if } |\sin(\psi_n^k)| \le \beta \end{cases}. \tag{18}$$

The control signal C_n^k which drives the error system to rest is then given by

$$\begin{aligned} C_n^k &= \widetilde{K}_n^k - K^k \\ &= \begin{cases} \frac{-2\pi}{\sin(\psi_n^k)}\left\{1 - \Omega^k - \mathrm{sgn}(\mathbf{G}^k\mathbf{X}_n) * \min(|\mathbf{G}^k\mathbf{X}_n|, \alpha)\right\} - K^k, & \text{if } |\sin(\psi_n^k)| > \beta \\ -K^k, & \text{otherwise} \end{cases}. \end{aligned} \tag{19}$$

4. Results

The case of uniform flow ($\mathrm{Re} = 100$) over a cable oscillating transversely (in y–z plane) to the oncoming flow in standing wave motion is used as the uncontrolled flow in the CML model. The cable mode shape, $L/D = 62$ and cable amplitude $A/D = 0.68$ are matched with the parameters in the numerical simulations of Newman and Karniadakis [9]. Other input parameters include $\Omega = 0.99$, $K_0 = 0.1$ and $k^* = 41$. Further details will be discussed when the wake patterns for this uncontrolled flow are presented.

In contrast to the other two control methods where energy methods are used to design optimal feedback gain matrices, the simple nature of the proportional control method means that the input feedback gain parameter γ, which is spatially and temporally invariant, must be optimized through a parametric study. The effect of the variation of the feedback gain parameter is shown in figure 2. In order to determine control effectiveness we define an average deviation of the phase of vortex shedding from the target as

$$\delta = \frac{\sum_{k=1}^{k^*} |\widehat{X}_{n\,\mathrm{final}}^k - \overline{X}|}{k^*}. \tag{20}$$

In the range $0.6 < \gamma < 1.0$, δ is small because the wake is controlled, and periodic patterns similar to the parallel shedding patterns shown in figure 3b are obtained. When $\gamma > 1.0$, larger values of δ result because other periodic states away from the target state are activated. After this optimization study, $\gamma = 0.9$ was chosen as the input feedback gain parameter for all presented results using proportional control.

The input parameters for the adaptive proportional control method are $\mathbf{P}_{-1} = \mathbf{P}_0 = 0.01\mathbf{I}_{k^*}, \mathbf{R} = \mathbf{I}_{k^*}$ where $\mathbf{I}_{k^*}$ is the identity matrix of dimension k^*. The main input parameter for the DNL control method is $\sigma_{\max}$, the maximum eigenvalue of the matrix (**A-AG**). The parameter $\sigma_{\max}$ determines the speed at which convergence to target state is achieved. The eigenvalues of this matrix are distributed randomly in a circle with radius $\sigma_{\max}$ from 0 to $\sigma_{\max}$. The parameter $\sigma_{\max}$ lies inside the unit circle of the complex plane. Other input parameters used in the DNL control methods include $\sigma_{\max} = 0.9$, $\beta = 0.1$, $\alpha = 0.006$. In §4.1–§4.4, we will make a comparative study of vortex shedding patterns, local dynamics, global dynamics and cable dynamics after the application of the three different control methods.

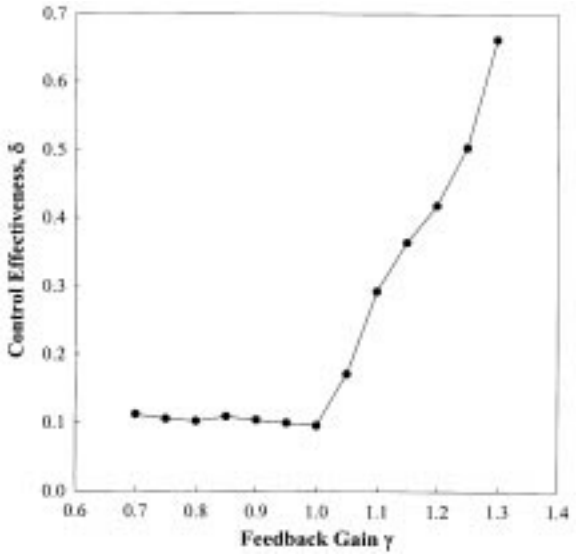

Figure 2. Optimization of the feedback gain parameter used in the proportional control signal. Control effectiveness, δ, is defined as the steady state mean deviation of the phase of vortex shedding from the target in (19).

4.1 *Vortex shedding patterns*

The uncontrolled flow case discussed earlier in this section results in vortex dislocations near the cable vibration nodes (figure 3a). Vortex shedding patterns from one shear layer are shown. The patterns are viewed by an observer looking in the transverse (y) direction observing the x–z plane (see figure 1). The cable and freestream flow direction (bottom to top) are included to orient the reader. The goal of the control schemes will be to steer the complex wake system to realize ordered, parallel patterns of vortex shedding. It has been shown [6] that parallel (2-D) vortex shedding patterns are predicted by the CML when a rigid cylinder is forced to oscillate in the 1/1 lock-on region (see figure 3b). This vortex shedding pattern serves as the target state ($\overline{X}^k = \eta = 0.9$) for the control studies.

In figure 4a proportional control techniques are applied to the uncontrolled flow. Complex wake structures such as the vortex dislocations in figure 3a are eliminated and periodic patterns similar to the targeted parallel shedding patterns result after proportional control is activated. The shedding patterns are not precisely parallel; instead they resemble the lace-like structures identified by Newman and Karniadakis [9]. We believe this is due to the absence of a span-wise varying feedback gain for proportional control. The application of adaptive proportional control or DNL control seeks to correct this situation.

We have achieved the desired parallel shedding patterns using adaptive proportional control as shown in figure 4b. When the DNL control signal is activated, ordered parallel vortex shedding patterns (figure 4c) are achieved. It will be shown in later sections that there is an improvement in targeting accuracy for the DNL method over the proportional control method, and in targeting speed over the adaptive proportional control method.

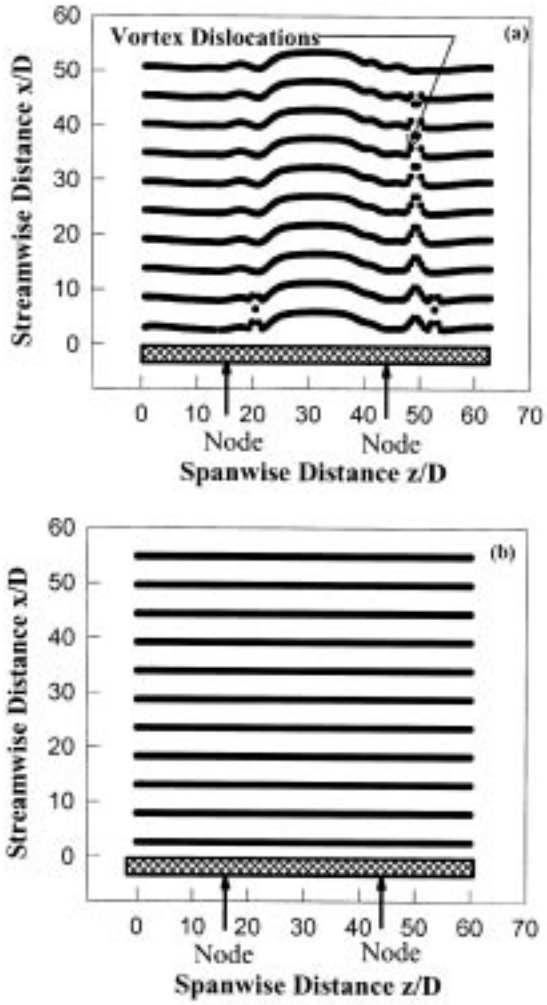

Figure 3. (**a**) Uncontrolled wake pattern showing vortex dislocations, uniform flow, $\Omega = 0.99$, $K_0 = 0.1$. (**b**) Parallel shedding patterns used as target state $\overline{X} = \eta = 0.9$. Rigid cylinder in uniform flow, $\Omega = 0.95, K^k = 0.9$ (within the lock-on region).

4.2 *Local dynamics*

The temporal dynamics of a wake can be clearly represented by the successive iterates of the phase of the vortex shedding event at a particular span-wise location, $\widehat{X}_n^k$. In figure 5a we plot the variable $\widehat{X}_n^{15}$ in case of proportional control, corresponding to a point near the cable midspan, i.e., $z/D = 21.7$ and $k = 15$. The variable $\widehat{X}_n^{15}$ for the uncontrolled wake $(0 < n < 600)$ exhibits chaotic dynamics with a positive Lyapunov exponent $= 0.118 \pm 0.044$ [31]. The proportional control signal is activated at $n = 600$. After approximately 50 iterates of the map, $\widehat{X}_n^{15}$ reaches a steady state value, $\widehat{X}_{n\,\text{final}}^{15} = 0.3266$, consistent with

the periodic shedding pattern of figure 4a. We note that this steady state value varies significantly from the target state $\overline{X}^k = \eta = 0.9$.

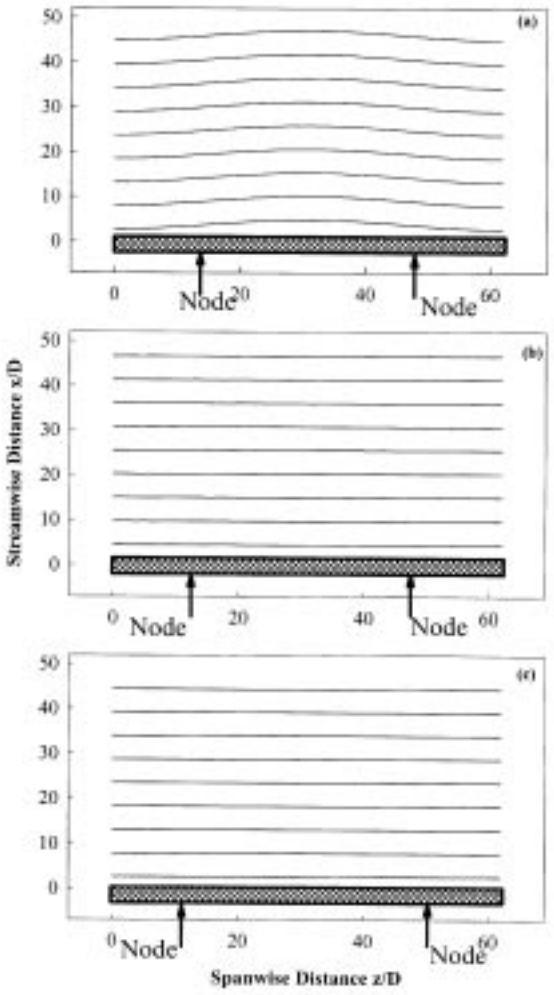

Figure 4. (**a**) Lace-like vortex shedding pattern after proportional control is activated. $\Omega = 0.99$, $K_0 = 0.1$, $k^* = 41$, $L/D = 62$, Re $= 100$, $U_c/U_\infty = 0.88$, $\varepsilon = 0.0247$, $A/D = 0.68$ at antinode, $\gamma = 0.9$. (**b**) Parallel (2-D) vortex shedding patterns after adaptive proportional control is activated. $\Omega = 0.99$, $K_0 = 0.1$, $k^* = 41$, $L/D = 62$, Re $= 100$, $U_c/U_\infty = 0.88$, $\varepsilon = 0.0247$, $A/D = 0.68$ at antinode, $\mathbf{P_o} = 0.01\mathbf{I}$, $\mathbf{R} = \mathbf{I}$. (**c**) Parallel (2-D) vortex shedding patterns targeted after DNL control is activated. $\Omega = 0.99$, $K_0 = 0.1$, $k^* = 41$, $L/D = 62$, Re $= 100$, $U_c/U_\infty = 0.88$, $\varepsilon = 0.0247$, $A/D = 0.68$ at antinode, $\eta = 0.5$, $\sigma_{\max} = 0.9$, $\beta = 0.1$, $\alpha = 0.006$. Freestream flow direction is from bottom to top for all vortex shedding patterns presented in this paper.

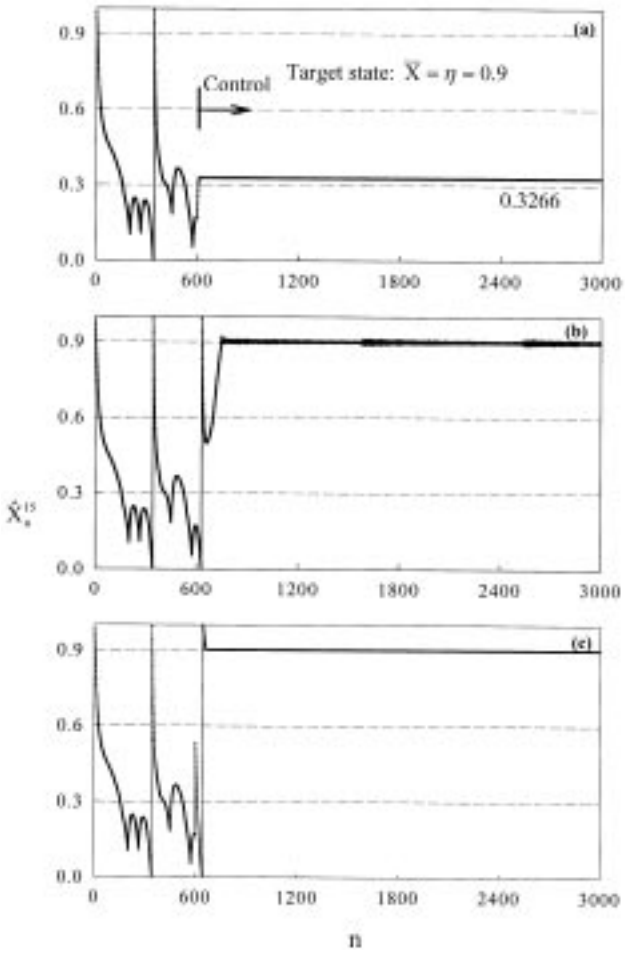

Figure 5. Temporal variation of the phase of vortex shedding $\widehat{X}_n^{15}$ at $k = 15$, $z/D = 21.7$. Control turned on at $n = 600$. (**a**) Proportional control, (**b**) adaptive proportional control and (**c**) DNL control.

The same variable, $\widehat{X}_n^{15}$, is then studied using the adaptive proportional control method (figure 5b). The adaptive proportional control signal is again activated at $n = 600$. After approximately 100 iterations of the map, $\widehat{X}_n^{15}$ reaches the target state, $\overline{X} = \eta = 0.9$, within 1% accuracy. This result is consistent with the parallel shedding observed in figure 4b. The phase dynamics of a span-wise oscillator, $\widehat{X}_n^{15}$, before and after DNL control activation is studied in figure 5c. The variable $\widehat{X}_n^{15}$ reaches the target state of $\overline{\mathbf{X}} = \eta = 0.9$ within a few shedding cycles of control activation. There is an improvement in targeting accuracy over the proportional control method and also an improvement in targeting speed and accuracy over the adaptive proportional control method.

The temporal variation of the proportional control signal, C_n^{15}, at the same span-wise location is shown in figure 6a and compared with the adaptive proportional control signal

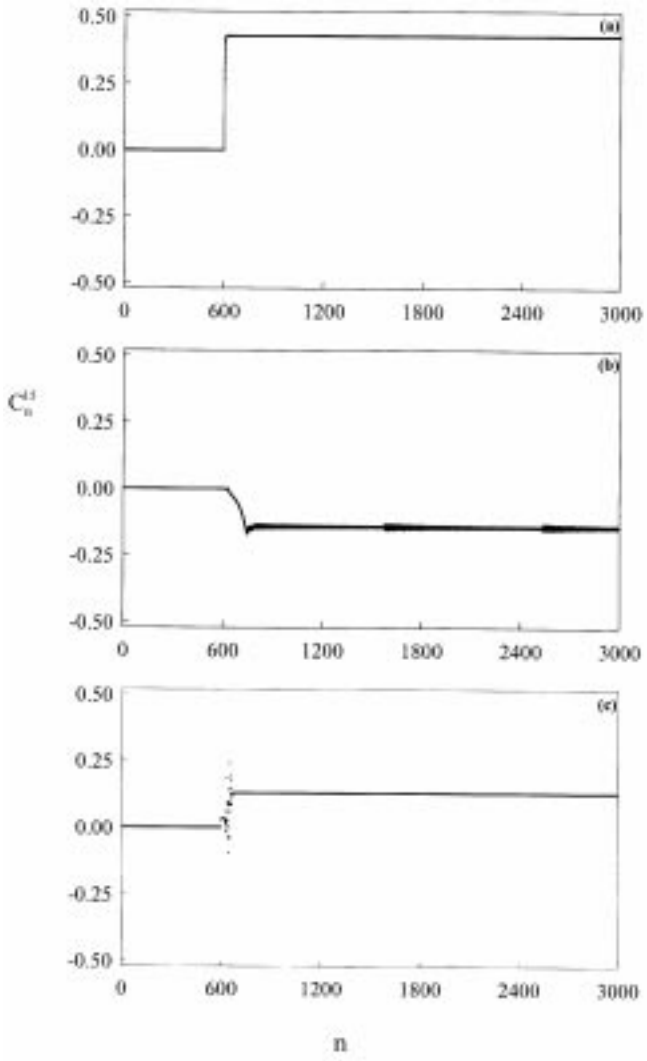

Figure 6. Temporal variation of the control signal C_n^{15} at $k = 15$, $z/D = 21.7$. (**a**) Proportional control, (**b**) adaptive proportional control and (**c**) DNL control.

and the DNL control signal in figures 6b and 6c respectively. The magnitude of the adaptive proportional control signal at this spatial location C_n^{15} (figure 6b) is less than the required proportional control signal for the same spatial location. The DNL control signal C_n^{15} shows an initial spike (figure 6c) with the signal magnitude larger than the corresponding adaptive proportional control signal values, but the control signal quickly settles down to a lower constant value once targeting is achieved.

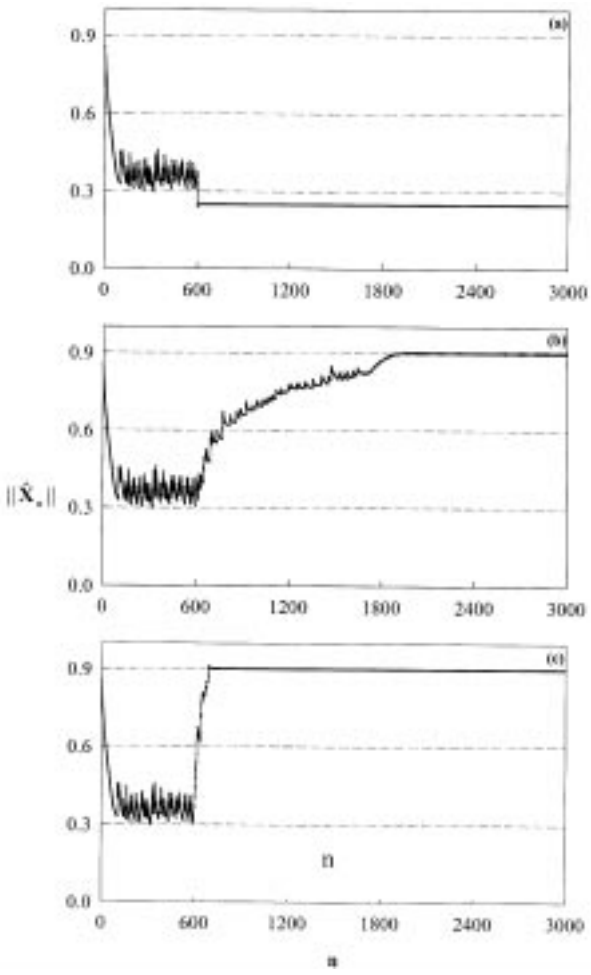

Figure 7. Temporal variation of the norm of the system variable, $||\widehat{\mathbf{X}}_n||$. (**a**) Proportional control, (**b**) adaptive proportional control and (**c**) DNL control.

4.3 *Global dynamics*

The local dynamics in §4.2 has highlighted certain features of the control schemes; however, study of the behavior of all k^* oscillators (i.e. the global dynamics) will yield further insight. The targeting accuracy over the spatial domain is studied using the spatial norm of the phase of the vortex shedding event, $||\widehat{\mathbf{X}}_n||$, defined as

$$||\widehat{\mathbf{X}}_n|| = \sqrt{\frac{\sum_{k=1}^{k=k^*} (\widehat{X}_n^k)^2}{k^*}}. \tag{21}$$

This variable is studied in figure 7a for the proportional control case. The variable $||\widehat{\mathbf{X}}_n||$ reaches a steady state value, $||\widehat{\mathbf{X}}_{n\,\mathrm{final}}|| = 0.2489$, within a few iterations of control

activation. Here $n\text{final} = 3000$. This value is different from $\widehat{X}^k_{n\,\text{final}} = 0.3266$ (see figure 5a), further proving that ordered but not parallel shedding patterns are achieved with the proportional control method. After the adaptive proportional control signal is activated at $n = 600$, $||\widehat{\mathbf{X}}_n||$ reaches the target state, $\overline{X} = \eta = 0.9$ (figure 7b), after a few hundred map iterations. In the case of DNL control, the global variable, $||\widehat{\mathbf{X}}_n||$, reaches the exact value of $\overline{X} = \eta = 0.9$ in figure 7c. These results again indicate that precisely parallel shedding patterns are targeted once control is turned on for these two control cases.

The temporal variation of the spatial norm of the error system variable, $||\mathbf{X}_n||$, (defined in §3.2) for the case of proportional control is studied in figure 8a. The global variable, $||\mathbf{X}_n||$, reaches a constant non-zero value indicating that ordered shedding patterns deviating from the targeted parallel shedding patterns are obtained using the proportional control method. The same variable is driven to zero when adaptive proportional control (figure 8b) is activated. In the case of DNL control (figure 8c) the spatial norm of the error system variable, $||\mathbf{X}_n||$, is again driven to zero after control is applied, once again confirming the resulting parallel shedding patterns. A dramatic improvement in targeting speed is shown for the DNL technique compared to the adaptive proportional method. The DNL technique achieves control within approximately 100 iterations while the adaptive proportional method requires approximately 1400 iterations.

The spatial norm of the control signal at each time step, $||\mathbf{C}_n||$, represents the energy input used to drive the system to a desired target state. This variable reaches a constant value of 0.3355 in figure 9a for the case of proportional control. The spatial norm of the adaptive proportional control signal $||\mathbf{C}_n||$ reaches a value of 0.2146 in figure 9b, 36% less than the value obtained for the proportional control method. The temporal variation of the norm of the control signal, $||\mathbf{C}_n||$, near $n = 600$ in figure 9c shows the complexity of the DNL control logic. The steady state magnitude of the norm of the control signal, $||\mathbf{C}_{n\,\text{final}}||$, was found to be lowest for the DNL logic with a value of 0.0987 (from figure 9c). This value is comparable to the amplitude of K_0.

4.4 *Cable dynamics*

Previous results have focused on local and global wake dynamics. In this section the cable dynamics are addressed. In figure 10a the spatial variation (along the cable span) of the steady state control signal, $C^k_{n\,\text{final}}$, is studied. For the three control methods, a sinusoidal variation in the magnitude of the control signal along the cable span in observed. In figure 10b the parameter $\widetilde{K}^k_{n\,\text{final}} = K^k + C^k_{n\,\text{final}}$, which is analogous to the steady state cable displacement, is presented. Addition of the control signal to the input K^k term results in a constant cable displacement amplitude along the cable span for the adaptive proportional and DNL methods. This implies that the cable oscillates as a rigid cylinder after control is applied. However, a variation in cable displacement along the cable span occurs for the proportional control case. These findings are consistent with earlier results. The adaptive proportional and DNL methods yielded parallel vortex shedding patterns after the control signal was applied as would be expected for flow over a rigid cylinder. The proportional control method yielded periodic, but lace-like, patterns consistent with a variation in cable displacement along the cable span.

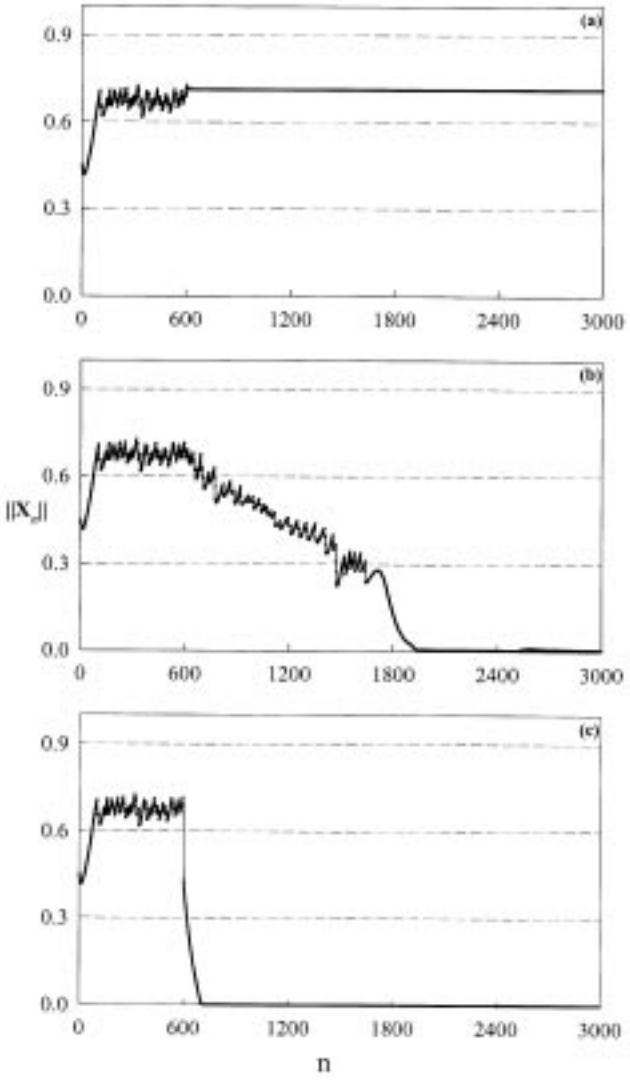

Figure 8. Temporal variation of the norm of the error system variable, $||\mathbf{X}_n||$. (**a**) Proportional control, (**b**) adaptive proportional control and (**c**) DNL control.

To this point the presented results have focused on control for a single flow condition detailed in figure 3. In order to prove the effectiveness of the control techniques over a wider range of flow conditions, a series of model runs varying the frequency ratio Ω and amplitude K_0 ($\Omega = 0.99, K_0 = 0.1$; $\Omega = 0.98, K_0 = 0.2$ for example) were studied. These values placed the system dynamics just outside the lock-on region as shown in the amplitude–frequency diagram of figure 11 in order to obtain complex wake structures out of the uncontrolled coupled map lattice. The resulting cable displacement $\widetilde{K}^k_{n\,\mathrm{final}}$ is plotted against

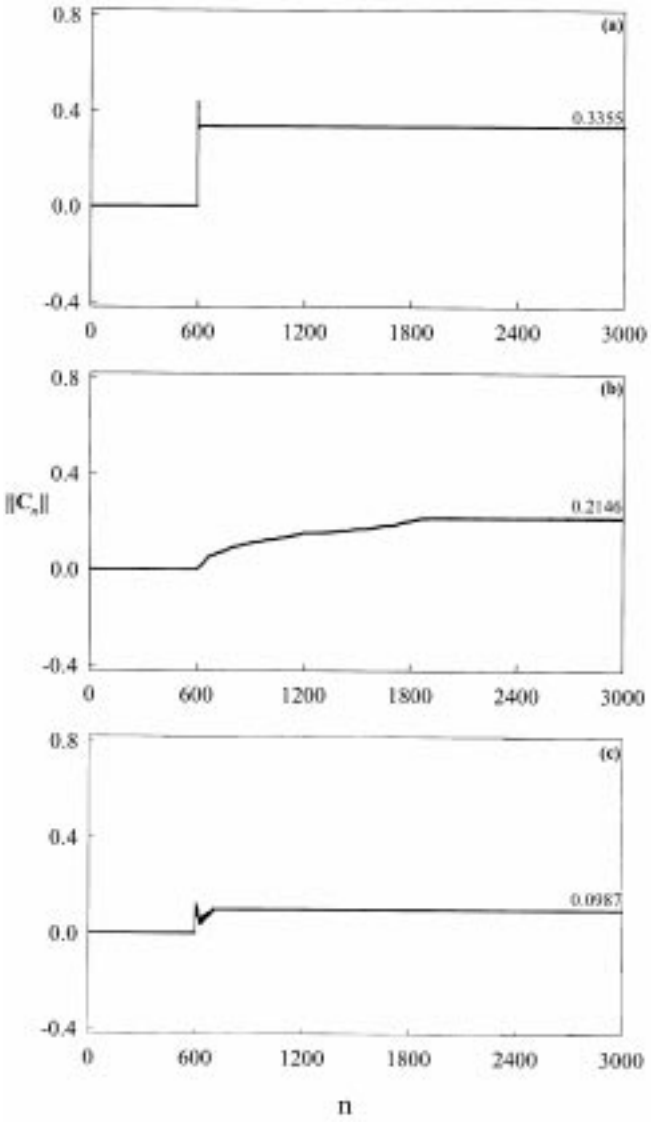

Figure 9. Temporal variation of the norm of control signal, $\|\mathbf{C}_n\|$. (**a**) Proportional control, (**b**) adaptive proportional control and (**c**) DNL control.

the frequency ratio Ω in the amplitude–frequency diagram of figure 11. A range of values must be plotted for the proportional control case due to the previously discussed variation in cable displacement amplitude for this case (see figure 10b). Single data points suffice for the adaptive proportional and DNL cases due to the constant cable displacement for these cases (see figure 10b).

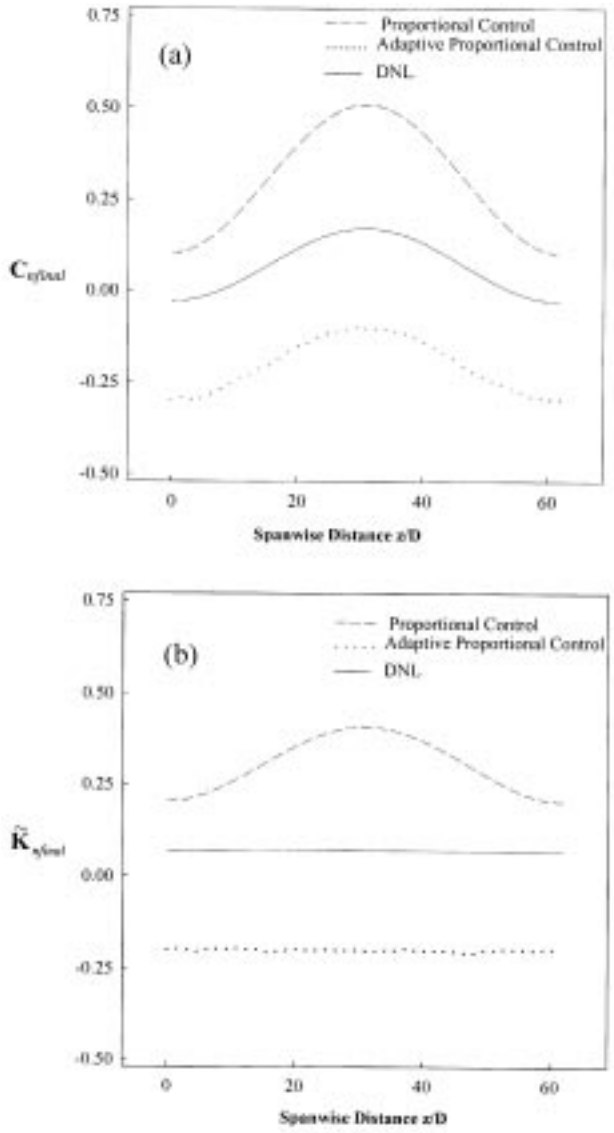

Figure 10. (**a**) Steady state span-wise variation of the control signal, $\mathbf{C}_{n\,\mathrm{final}}$. Proportional control (dashed line), adaptive proportional control (dotted line) and DNL control (solid line). (**b**) Steady state cable displacement $\widetilde{K}^{k}_{n\,\mathrm{final}}$ after control. Proportional control (dashed line), adaptive proportional control (dotted line) and DNL control (solid line).

The solid lines in figure 11 denote the boundary of the 1/1 lock-on region for the temporal circle map in eq. (1). It is observed that all the three control methods achieve the targeted state by forcing the system into the periodic 1/1 lock-on region of the circle map.

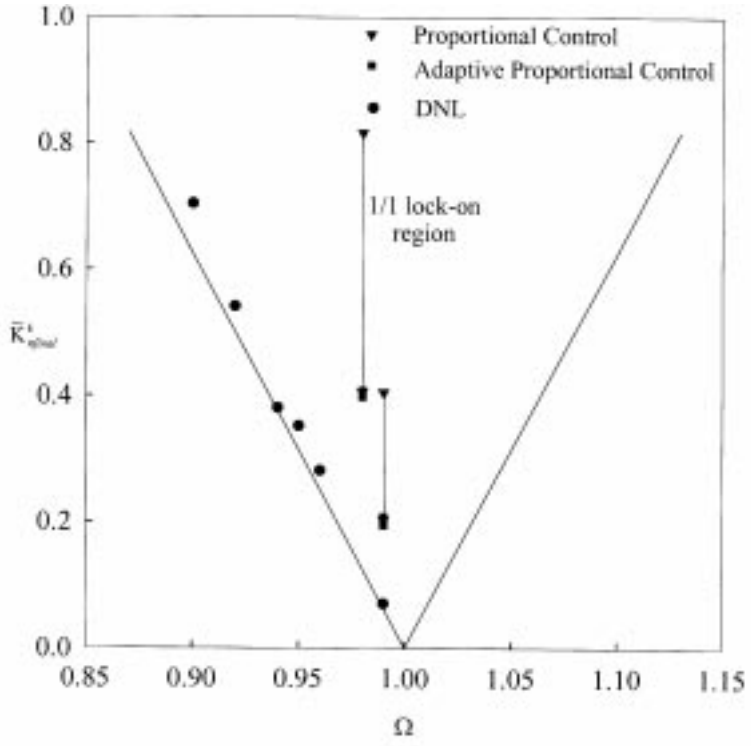

Figure 11. Circle map lock-on region showing constant span-wise cable oscillation amplitudes after adaptive proportional and DNL control activation, and the cable oscillation amplitude range after proportional control activation. The cable amplitude after control, $\widetilde{K}^k_{n\,\mathrm{final}}$, is driven into the lock-on region consistent with periodic shedding behavior.

The efficiency of the DNL method is highlighted in figure 11. The DNL method incorporates the minimum control signal necessary to drive the system just beyond the boundary of the lock-on region. The other two control methods require larger amplitude control signals that drive the system further into the lock-on region. Largest cable amplitudes are required for the proportional control case to be consistent with figure 9. Thus, the dynamics of the controlled system can be interpreted from a dynamical systems perspective by correlating the control signal with the behavior of the temporal circle map.

5. Conclusions

Control terms have been added to a previously developed coupled map lattice [6]. Complex three-dimensional vortex shedding patterns predicted by CML, such as vortex dislocations were controlled, and ordered parallel (2-D) vortex shedding patterns and lace-like patterns were established. Three different control schemes were applied to the CML model.

The resulting models can be used to compare the control effectiveness of different control schemes. The model based on non-linear control theory was most effective in controlling the complex wake and targeting parallel shedding patterns predicted by the coupled map lattice. The DNL technique required lower control signal amplitudes than the other two control techniques. The adaptive proportional control method was also effective in controlling the complex wake and targeting parallel shedding patterns. However, this method required larger control signals and longer targeting times to achieve control. A proportional control method was also used to control complex wake structures predicted by the coupled map lattice. However, in this case only periodic lace-like patterns were achieved after control. This limitation of the proportional control method was overcome by designing a spatially (and temporally) adaptive feedback gain matrix for the other two control methods. Finally, the wake structures were correlated to the classical lock-on behavior of the standard circle map using our dynamical systems approach.

As discussed earlier, the CML models developed are suitable for real-time implementation in future wake experiments with further development. The experimental methods by which the flow will be sensed and the control input actuated require further study. This implementation will be aided by the efficiency of the CML models. The CML models require 10^{-1} wall clock seconds per shedding cycle on a Pentium PC, while the numerical simulation of [9], for example, requires approximately 10^4 wall clock seconds per shedding cycle on an IBM supercomputer for the same flow. In addition, sheared free-stream flows will also be studied with the CML models. Oblique shedding patterns (vortex lines oriented obliquely to cylinder axis) that are commonly observed in experimental wake studies will serve as the target states.

Acknowledgments

This work was supported by the Office of Naval Research (Grant No. N00014-96-1-0004) under the direction of Dr Thomas Swean.

References

[1] P Bearman, *Ann. Rev. Fluid Mech.* **16**, 195 (1984)
[2] C H K Williamson, *J. Fluid Mech.* **328**, 345 (1996)
[3] M J Feigenbaum, L P Kandanoff and S J Shenker, *Physica* **D5**, 370 (1982)
[4] S J Shenker, *Physica* **D5**, 405 (1982)
[5] S Ostlund, D Rand, J Sethna and E Siggia, *Physica* **D8**, 303 (1983)
[6] D J Olinger, *Phys. Fluids* **A10**, 1953 (1998)
[7] O M Griffin and S E Ramberg, *J. Fluid Mech.* **66**, 553 (1974)
[8] D Yoerger, M Grosenbaugh, M Triantafyllou and J Burgess, *J. Offshore Mech. Arctic Engg.* **113**, 117 (1991)
[9] D J Newman and G E Karniadakis, *J. Fluid Struct.* **10**, 439 (1996)
[10] D J Newman and G E Karniadakis, *J. Fluid Mech.* **344**, 95 (1997)
[11] K Kaneko, *Physica* **D37**, 60 (1989)
[12] K Kaneko, *Physica* **D54**, 5 (1991)
[13] D J Olinger, A B Chhabra and K R Sreenivasan, *Pramana – J. Phys.* **48**, 693 (1997)
[14] L D Landau and E M Lifshitz, *Fluid mechanics: Course in theoretical physics* (Pergamon, Oxford, 1959)
[15] J T Stuart, *J. Fluid Mech.* **9**, 353 (1960)

[16] K R Sreenivasan, P J Strykowski and D J Olinger, Hopf bifurcation Landau equation, and vortex shedding behind circular cylinders, in *ASME forum on unsteady flow separation*, FED **52**, 1 (1987)
[17] M Provensal, C Mathis and L Boyer, *J. Fluid Mech.* **182**, 1 (1987)
[18] J E Marsden and M McCracken, *The Hopf bifurcation and its applications* (Springer-Verlag, New York, 1976)
[19] C H K Williamson, *J. Fluid Mech.* **206**, 579 (1989)
[20] M Hammache and M Gharib, *J. Fluid Mech.* **232**, 567 (1991)
[21] M P Davis, Low-order modeling of freely vibrating flexible cables (MS Thesis, Worcester Polytechnic Institute, Worcester, MA, USA, 2001)
[22] E Ott, C Grebogi and J A Yorke, *Phys. Rev. Lett.* **64**, 1196 (1990)
[23] S Sinha and N Gupta, *Phys. Rev.* **E58(5)** (1998)
[24] J Singer, Y Z Wang and H Bau, *Phys. Rev. Lett.* **66**, 1123 (1991)
[25] Y Wang, J Singer and H Bau, *J. Fluid Mech.* **237**, 479 (1992)
[26] P K Yuen and H Bau, *Phys. Fluids* **11**, 135 (1999)
[27] G Balasubramanian, *Control of complex cylinder wake structures using coupled map lattices*, MS Thesis, Worcester Polytechnic Institute, Worcester, MA, USA (1998)
[28] W J Rugh, *Linear system theory* (Prentice-Hall, Englewood Cliffs, NJ, USA, 1995)
[29] M Gad-el-Hak, *Flow control: Passive, active and reactive flow management* (Cambridge University Press, London, UK, 2000)
[30] G C Goodwin and K S Sin, *Adaptive filtering, prediction and control* (Prentice-Hall, Englewood Cliffs, NJ, USA, 1984)
[31] J C Sprott, *Chaos data analyzer* (Physics Academic Software, Raleigh, NC, USA, 1992)